

# Dopamine Imaging in Living Cells and Retina by Surface-Enhanced Raman Scattering Based on Functionalized Gold Nanoparticles

Xueqian Ren,<sup>||</sup> Qingwen Zhang,<sup>||</sup> Jinglei Yang,<sup>||</sup> Xinjuan Zhang, Xueming Zhang, Yating Zhang, Liping Huang, Changshun Xu, Yuancai Ge, Hao Chen,<sup>\*</sup> Xiaohu Liu,<sup>\*</sup> and Yi Wang<sup>\*</sup>



Cite This: <https://doi.org/10.1021/acs.analchem.1c01108>



Read Online

ACCESS |



Metrics & More

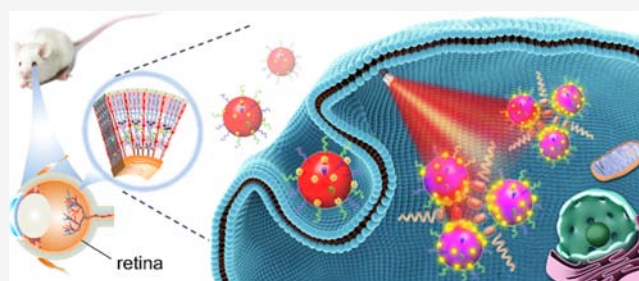


Article Recommendations



Supporting Information

**ABSTRACT:** Retinal dopamine is believed to be involved in the development of myopia, which is projected to affect almost half of the world population's visual health by 2050. Direct visualization of dopamine in the retina with high spatial precision is essential for understanding the biochemical mechanism during the development of myopia. However, there are very few approaches for the direct detection of dopamine in the visual system, particularly in the retina. Here, we report surface-enhanced Raman scattering (SERS)-based dopamine imaging in cells and retinal tissues with high spatial precision. The surface of gold nanoparticles is modified with *N*-butylboronic acid-2-mercaptoethylamine and 3,3'-dithiodipropionic acid di(*N*-hydroxysuccinimide ester), which shows excellent specific reaction with dopamine. The existence of dopamine triggers the aggregation of gold nanoparticles that subsequently form plasmonic hot spots to dramatically increase the Raman signal of dopamine. The as-synthesized SERS nanoprobe has been evaluated and applied for dopamine imaging in living cells and retinal tissues in form-deprivation (FD) myopia guinea pigs, followed by further investigation on localized dopamine levels in the FD-treated mice. The results suggest a declined dopamine level in mice retina after 2-week FD treatment, which is associated with the development of myopia. Our approach will greatly contribute to better understanding the localized dopamine level associated with myopia and its possible treatments. Furthermore, the imaging platform can be utilized to sensing other important small molecules within the biological samples.



## INTRODUCTION

Dopamine is an essential neurotransmitter that regulates many physiological behaviors of the central nervous systems. An appropriate level of dopamine in the brain could regulate motivation, movement, pleasure, and reward.<sup>1</sup> Abnormal levels of dopamine in the brain, however, may cause Alzheimer,<sup>2</sup> Parkinson,<sup>3</sup> and Schizophrenia diseases.<sup>4</sup> In the visual system, particularly, dopamine has been reported as well to be crucial in regulating visual signals and light adaptation, participating in the process of circadian rhythm and controlling eye growth.<sup>5</sup> Myopia as a global visual problem may cause fundus diseases such as macular degeneration, retinal degeneration, and even blindness.<sup>6</sup> It has been predicted that the myopia population and the high myopia population will increase to 49.8 and 9.8% of the world population, respectively, by 2050.<sup>7</sup> The level of dopamine in the retina has been reported to be downregulated after form-deprivation (FD)-induced myopia development in some animal models, indicating a strong correlation between dopamine and myopia.<sup>8,9</sup> Monitoring dopamine levels in the retina is thus very important for us to understand its molecular functions during the development of myopia and the biochemical mechanism of myopia, which in turn may suggest a dopamine-related treatment for myopia.<sup>8</sup> The current

commonly used method for the detection of dopamine in the retina is high-performance liquid chromatography (HPLC), which can only detect the total dopamine and is limited by the complicated procedures.<sup>9</sup> Therefore, the specific detection or mapping of dopamine with spatial resolution in biological samples is very much desired and helps to answer the role of dopamine for the development of myopia and other neuron-related diseases.

Surface-enhanced Raman scattering (SERS) is a promising analytical technology with ultrahigh sensitivity and selectivity.<sup>10</sup> It is widely used in various fields such as biomedicine, biochemistry, and environmental science.<sup>11,12</sup> The spectral signal of SERS generally contains fingerprint peaks, which intrinsically provide high selectivity for target analytes.<sup>11</sup> Meanwhile, SERS signals can be remarkably enhanced at the gap between the metal nanoparticles as "hotspot", even

Received: March 14, 2021

Accepted: July 12, 2021

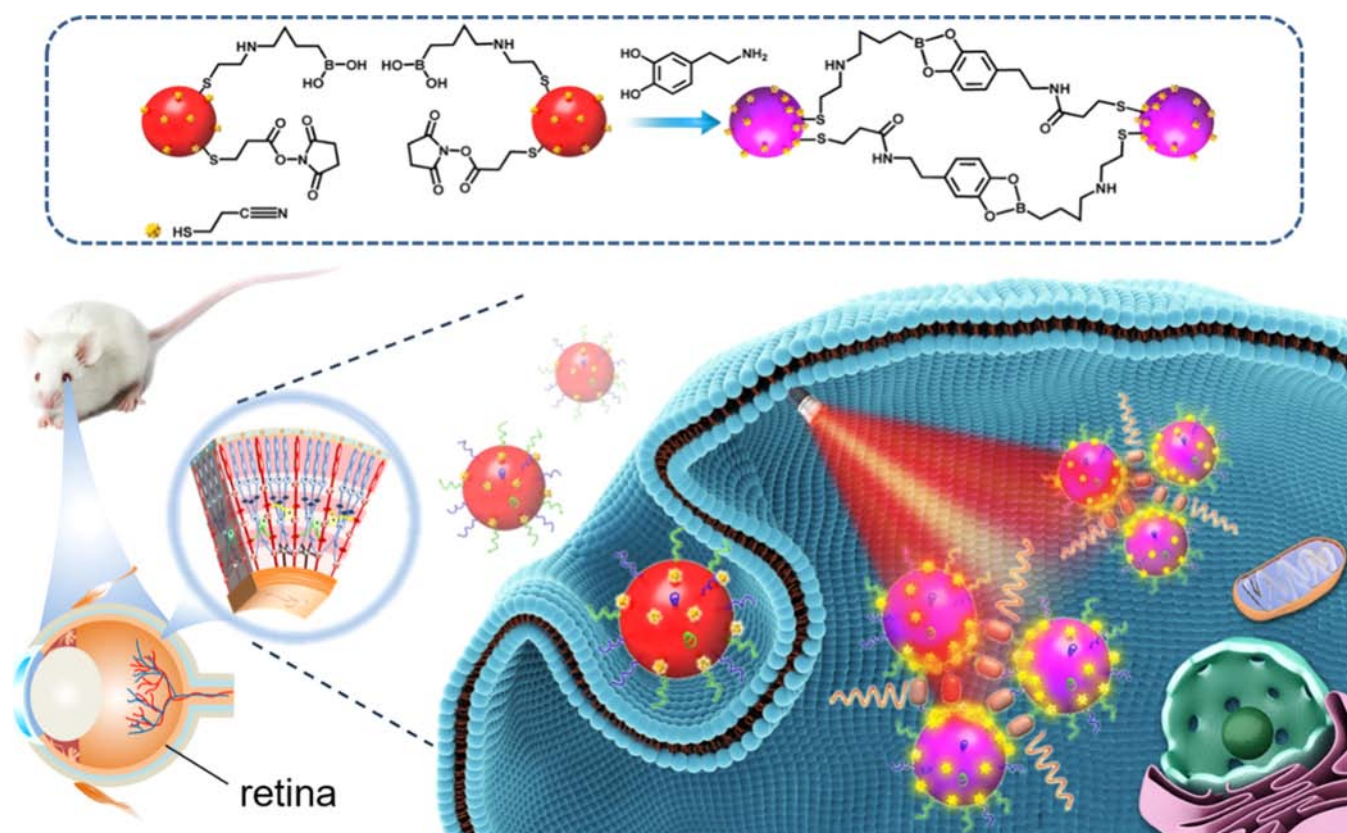


**Figure 1.** Schematic illustration of the SERS assay for local dopamine imaging based on functional AuNPs, which enables the formation of hotspots for subsequent cellular and retinal imaging.

realizing the single molecule detection.<sup>13</sup> Together with the fast optical controlled excitation and spectral acquisition, SERS is thus very suitable for tracing a tiny amount of specific analytes in biological samples and *in vivo* tests. Colloidal gold nanoparticles (AuNPs) as a well-established colorimetric sensing platform have already drawn much attention in the past decades, due to their high extinction coefficients and unique size-dependent optical property.<sup>14,15</sup> AuNPs can be easily functionalized with different molecules to target a broad spectrum of analytes via colorimetric responses,<sup>16</sup> fluorescence resonance energy transfer,<sup>17</sup> electrochemical responses,<sup>18</sup> and SERS.<sup>19</sup> Especially in the SERS-related assays, the hotspots for enhancement are formed upon the AuNP aggregation triggered by specific analytes. Moreover, with appropriate surface functionalization, AuNPs are generally much less toxic to be applied to cellular or tissue analysis where the biocompatibility is very much required.<sup>19</sup>

In this work, we aim to image dopamine in living cells and retinal tissues in animal models by using SERS to investigate the dopamine levels during the development of myopia. In order to introduce the hotspot for SERS and a biocompatible probe for cell internalization, AuNPs are chosen to be functionalized with boronic acid-terminated thiol molecules (*N*-butylboronic acid-2-mercaptoethylamine, BME) and amine-reactive succinimidyl residue molecules [3,3'-dithiodipropionic acid di(*N*-hydroxysuccinimide ester), DSP], which react with the two hydroxyl groups and aminol group of dopamine, respectively (Figure 1). The presence of dopamine triggers the reactions resulting in the agglomeration of AuNPs,<sup>20</sup> the formation of plasmonic hotspots, and thus the enhanced Raman scattering signals of dopamine. Further

delivery of functional AuNPs into living cells and retina would therefore indicate the local amount of dopamine (Figure 1). As a demonstration, we apply this SERS imaging assay to PC12 cells and guinea pig retina to evaluate the efficacy of our nanoprobes, followed by examining the local dopamine levels in retinal tissues of the FD-treated mice.

## EXPERIMENTAL SECTION

**Preparation of BME/DSP/SPN-Au and Detection of Dopamine.** The surfaces of the AuNPs were functionalized with BME, DSP, and 3-sulfanylpropanenitrile (SPN). 1  $\mu$ L of 2 mM BME, 1.6  $\mu$ L of 2 mM DSP, and 1.8  $\mu$ L of 2 mM SPN were added to 10 mL of AuNP dispersion and mixed under stirring at room temperature for 3 h. Then, AuNP solution was centrifuged at 5000 rpm for 10 min, which was resuspended in phosphate buffer (pH 7.4, 10 mM). A volume of 15  $\mu$ L dopamine at different concentrations (0, 0.005, 0.01, 0.05, 0.1, 0.5, and 1 mM) was added to 1.485 mL of the functionalized AuNP solution (0.1 nM) and incubated for 30 min at room temperature for further tests.

**SERS Imaging of Dopamine in Living Cells.** The cells were seeded in a 6 mm optical Petri dish at a concentration of  $5 \times 10^4$  cells/mL and cultured in an incubator under 5% CO<sub>2</sub> at 37 °C for 24 h. The Petri dish was then washed with PBS (1 $\times$ , pH 7.4) to remove dead cells. The cells were incubated with ghrelin (4.5  $\mu$ M) for 10 min. The Petri dish was then washed with PBS (1 $\times$ , pH 7.4). Functionalized AuNPs (0.1 nM) and ghrelin (4.5  $\mu$ M) were then added to the fresh culture medium and incubated with the cells for 8 h. The Raman imaging was carried out under the condition of a 17 mW He–Ne laser (632.8 nm) and a L50 $\times$  objective lens. The

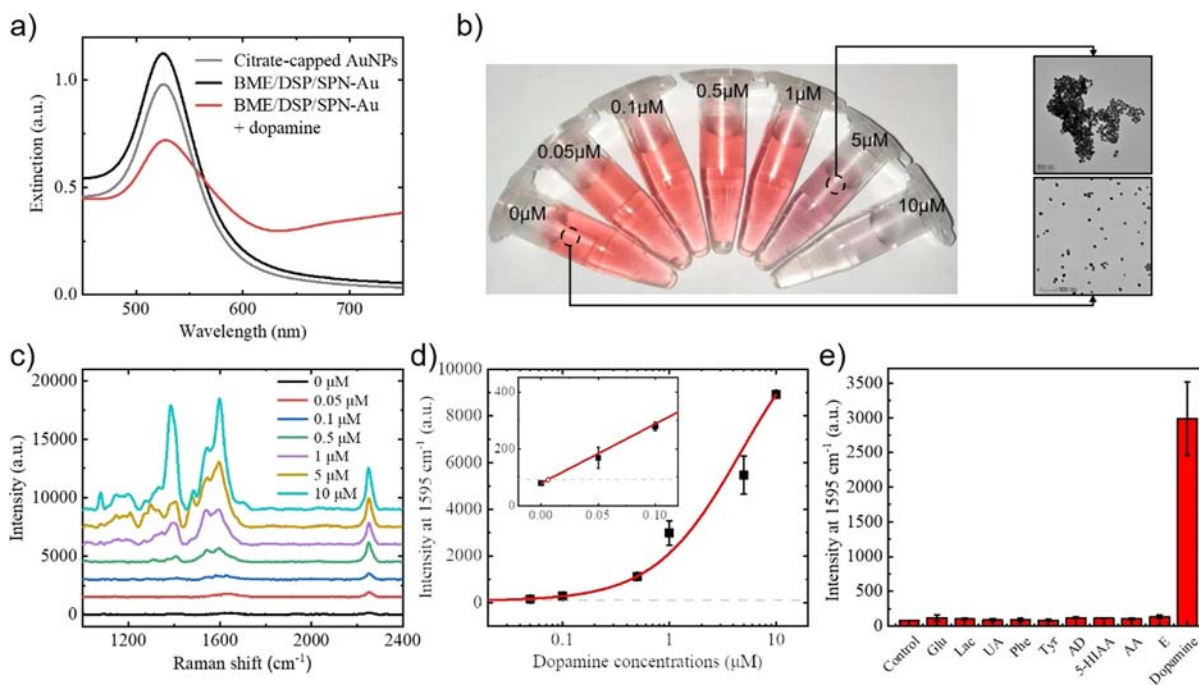


**Figure 2.** Characterization of dopamine detection using BME/DSP/SPN-Au probes. (a) UV–vis spectra of the citrate-capped AuNPs (gray), the functionalized BME/DSP/SPN-Au probes before (black) and after (red) addition of dopamine ( $5 \mu\text{M}$ ). (b) Photograph of the nanoprobes upon the addition of dopamine from 0 to  $10 \mu\text{M}$ , the corresponding TEM images as indicated. (c) SERS spectra of the nanoprobes upon the addition of different concentrations of dopamine (0– $10 \mu\text{M}$ ). (d) Plot of intensities at  $1595 \text{ cm}^{-1}$  vs different concentrations of dopamine, fitted with a red curve. A broken gray line represents three times of standard deviation for LOD estimation. (e) Histogram of Raman intensities at  $1595 \text{ cm}^{-1}$  in the presence of different substances at  $1 \mu\text{M}$ .

scan scale was set at  $1 \mu\text{m}$  per step with an integration time of 1 s (single PC12 cell) and  $1.5 \mu\text{m}$  per step with an integration time of 0.5 s (multiple PC12 cells). The 3D images of cells were obtained with different “z-slice” spaced  $1 \mu\text{m}$  apart.

**SERS Imaging of Retinal Dopamine.** On the morning after 3-day or 2-week FD, the translucent lens or facemask was taken off and the nanoprobes were injected into the subretinal space of the right eye of the animal models. The same amount of nanomaterials was injected in the normal control group. Animals were sacrificed 15 h after the injection. The retinal whole mount was obtained on ice after removal of cornea and lens. The Raman imaging was done by the Renishaw Confocal Raman system and performed under the condition of a 17 mW He–Ne laser ( $632.8 \text{ nm}$ ) and a  $\text{L50}\times$  objective lens. The scan scale was set at  $1 \mu\text{m}$  per step for a small area and  $1.5 \mu\text{m}$  per step for a large area with an integration time of 0.5 s.

## RESULTS AND DISCUSSION

### Characterization of the Functionalized AuNP Probes.

Citrate-capped AuNPs with 40 nm in diameter were synthesized and considered as the favorable size of particles for cellular uptake.<sup>21</sup> The UV–vis spectrum of the as-synthesized AuNPs showed the absorbance peak at 526 nm, indicating the nanoparticles size of 40 nm. The narrow peak of the spectrum also indicated the high quality of AuNPs in terms of good monodispersity and size distribution (Figure 2a, gray curve). The DLS results showed an average and centralized size at around 40 nm, which was consistent with the results measured by the UV–vis spectrum (Figure S1a). The AuNPs were then surface-modified and stabilized with the mixture of three thiolated molecules: BME, DSP, and SPN in an optimized ratio of 1:1.6:2. The stable boronate complex

could be formed between boronic acid in BME and diols in dopamine; meanwhile, the succinimidyl entity in DSP could be easily replaced by the amine group in dopamine to form an amide bond. BME and DSP were therefore served not only as stabilizers but also as recognizers to selectively bind dopamine on different sites, which enabled the subsequent aggregation of AuNPs and color changes upon the addition of dopamine. SPN was utilized as a SERS signal indicator and would be discussed in the later section. Compared with citrate-capped AuNPs, no observable change was found in the absorbance peak wavelength ( $526 \text{ nm}$ ) after the modification with BME/DSP/SPN (BME/DSP/SPN-Au) (Figure 2a, black curve). It is reasonable, as the thiolated molecules were comparable with citrates in size, thus, very limited refractive index change occurred on the surface of AuNPs.<sup>22</sup>

The functionalized AuNP probes for dopamine detection were characterized with colorimetry and SERS. The nanoprobes were incubated with  $5 \mu\text{M}$  dopamine for a period of 30 min and recorded with an UV–vis spectrometer. As a result, the absorbance at  $526 \text{ nm}$  decreased significantly, whereas the absorbance at  $686 \text{ nm}$  increased (Figure 2a, red curve). Control experiments were done by functionalizing the AuNPs with either BME/SPN (BME/SPN-Au) or DSP/SPN (DSP/SPN-Au), followed by the same testing procedure. The UV–vis results showed no observable changes after adding  $5 \mu\text{M}$  dopamine due to the lack of the cross-linking effect, which required the presence of both BME and DSP on the surface of AuNPs (Figure S1b). Moreover, the Raman spectrum was dramatically enhanced after the addition of dopamine especially at  $1480/1595$  and  $2251 \text{ cm}^{-1}$  referring to the benzene ring in dopamine molecules and nitrile group in SPN, respectively (Figure S1c). The similar control experiments of functionalized AuNPs were done as the colorimetric assay, and

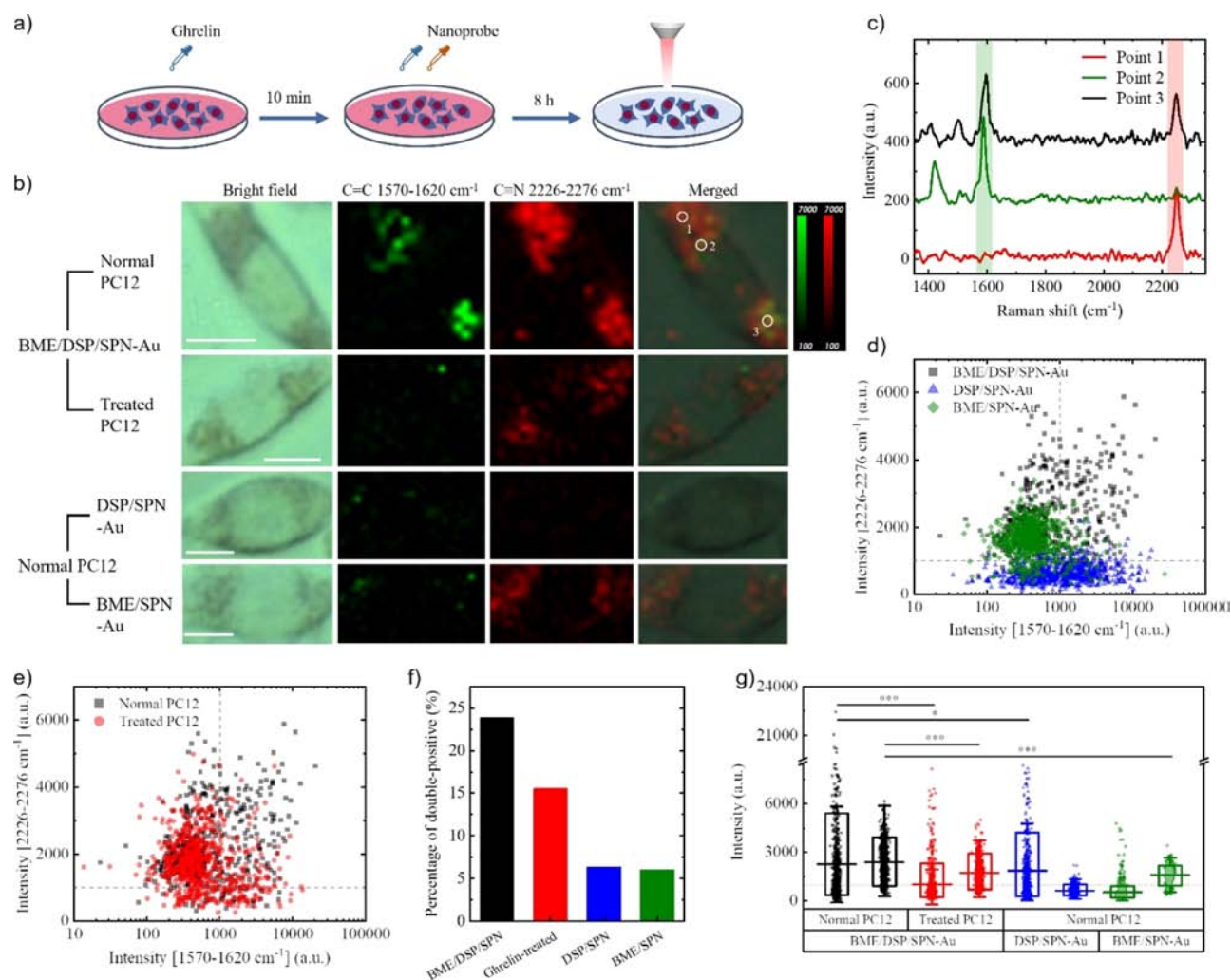


**Figure 3.** SERS imaging analysis of dopamine in PC12 cells incubated with functional nanoprobe. (a) Schematic illustration for PC12 cells treated with ghrelin and incubated with BME/DSP/SPN-Au or control nanoparticles prior to Raman imaging. (b) Bright-field, SERS mapping images of differently treated single living cells acquired in 1570–1620 and 2226–2276  $\text{cm}^{-1}$  channels and their merged images. From top to bottom: PC12 cells incubated with BME/DSP/SPN-Au; ghrelin-pretreated PC12 cells incubated with BME/DSP/SPN-Au; PC12 cells incubated with DSP/SPN-Au, and BME/SPN-Au. Scale bar: 10  $\mu\text{m}$ . (c) SERS spectra of point 1, point 2, and point 3 in (a), respectively. (d) Scatter plot of pixel intensities in Raman images of normal PC12 cells incubated with BME/DSP/SPN-Au (black squares), DSP/SPN-Au (blue triangles), and BME/SPN-Au (green diamonds), respectively. (e) Similar scatter plot as in (d) of normal PC12 cells (black squares) and ghrelin-treated PC12 cells (red circles), both incubated with BME/DSP/SPN-Au. (f) Percentages of double-positive pixels in all derived pixels. From left to right: PC12 cells incubated with BME/DSP/SPN-Au (black); ghrelin-pretreated PC12 cells incubated with BME/DSP/SPN-Au (red); PC12 cells incubated with DSP/SPN-Au (blue), and BME/SPN-Au (green). (g) Box plot of pixel intensities in Raman images of each group in the same order as in (f). Within each group, the left and right boxes showed the averaged intensities in 1570–1620 and 2226–2276  $\text{cm}^{-1}$  channels, respectively.

BME/SPN-Au and DSP/SPN-Au showed a relatively weak Raman signal ( $<600$  a.u.) at about 1595  $\text{cm}^{-1}$  upon the addition of 5  $\mu\text{M}$  dopamine (Figure S1d), which is mainly ascribed to the bind of dopamine on the surface of AuNPs but without the trigger of aggregations. The BME/DSP/SPN-Au was therefore demonstrated as the effective nanoprobe for dopamine detection.

In order to estimate the limit of detection (LOD), various concentrations of dopamine (0–10  $\mu\text{M}$ ) solutions were added into the AuNPs. The colors of the functionalized AuNPs gradually changed from wine red to purple in a concentration-dependent manner due to the induced particle aggregations, which was confirmed by transmission electron microscopy (TEM) (Figure 2b). The UV–vis spectra showed the same trend as color changes. The featured peak intensity at 526 nm dropped significantly, while a broadened peak at around 686

nm ascended (Figure S2a). The calibration curve based on the ratio of absorbance at 686 and 526 nm ( $A_{686}/A_{526}$ ) showed the LOD of 0.1  $\mu\text{M}$  on the detection of dopamine (Figure S2b). The SERS spectra showed similar results as the colorimetric assay (Figure 2c). Specifically, the Raman intensity at 1480 and 1595  $\text{cm}^{-1}$  (corresponding to the stretching of the phenolic  $\text{CH}_2$  bonds and the  $\text{C}=\text{C}$  bond of the benzene ring, respectively) increased gradually, as the concentration of dopamine increased. The calibration curve based on the peak intensities at 1595  $\text{cm}^{-1}$  showed the LOD of 0.012  $\mu\text{M}$ , which was eightfold lower than the colorimetric assay (Figure 2d). The SERS assay thus would be effective for cellular dopamine detection and imaging, giving that the cytoplasmic concentration of dopamine was generally in the low  $\mu\text{M}$  range.<sup>23</sup>

The specificity of dopamine in the present assays was evaluated by incubating the nanoprobes with various substances (all at 1  $\mu\text{M}$ ) including glucose, lactate, uric acid, phenylalanine, tyrosine adenosine, 5-hydroxyindole-3-acetic acid, ascorbic acid, epinephrine, and dopamine for 30 min (Figure S3a). In the colorimetric assay, there was no detectable change of peak intensity at 526 nm for all other molecules except dopamine (Figure S3b). The absorbance difference ratio ( $\Delta A_{686}/A_{526}$ ) in the presence of dopamine was positive, compared to the negative results of others (Figure S3c), which suggested that our nanoprobes were selective for dopamine detection. The Raman spectra also showed that only the presence of dopamine caused significant enhancement of interested peaks in the Raman spectra (Figure S3d). The histogram was drawn by intensities at 1595  $\text{cm}^{-1}$  in the Raman spectra, confirming the high specificity of our nanoprobes for dopamine detection (Figure 2e).

**Dopamine Imaging in Living Cells.** The PC12 cell was a commonly used neuronal cell line that could synthesize neurotransmitters such as dopamine and norepinephrine.<sup>24</sup> It was therefore used as a model for dopamine imaging with AuNP probes. First, the cells after being treated with all tested concentrations of nanoprobes (0.04, 0.07, and 0.1 nM) showed that more than 90% of cells was viable compared with untreated cells (Figure S4a), indicating the low toxicity of AuNP probes. The highest concentration 0.1 nM of particles was then selected for maximizing the cellular dopamine responses. In addition, the internalization of the nanoprobes was examined by 3D Raman imaging of a single cell (Figure S4b), in which the SPN molecule was selected as the Raman tag because its nitrile group had a strong and narrow single peak (2251  $\text{cm}^{-1}$ ) in the cellular Raman-silent region (1800–2800  $\text{cm}^{-1}$ ). The Raman signals of the exogenous nitrile and the benzene from dopamine distributed across over first three layers ( $-6.6$  to  $-8.6$   $\mu\text{m}$ ) within the cell margin, suggesting that BME/DSP/SPN-Au had successfully entered PC12 cells and agglomerated accordingly. The Raman spectra derived from the 3D image (Figure S4c) revealed a sudden decrease of intensities at around 1595 and 2251  $\text{cm}^{-1}$  after the layer of  $-8.6$   $\mu\text{m}$  (Figure S4c), which was reasonable that the specific SERS signals appeared only in the intracellular volume.

After the evaluation of toxicity and cell internalization of our nanoprobes, details of SERS imaging for intracellular dopamine were studied. Functional BME/DSP/SPN-Au nanoprobes were incubated with PC12 cells or ghrelin-treated PC12 cells for 8 h, prior to SERS signal mapping of the nitrile group and benzene rings in single cell/multiple cells (Figure 3a). The Raman peaks of the benzene ring in dopamine and the nitrile group in SPN were previously found to be 1595 and 2251  $\text{cm}^{-1}$ , respectively, which might shift slightly within  $\pm 25$   $\text{cm}^{-1}$  due to the complex environment in cells. The imaging analysis was thus performed in two channels (1570–1620 and 2226–2276  $\text{cm}^{-1}$ ) according to the Raman peaks together with a bright-field view. Within the same cell (bright field), the benzene signal (1570–1620  $\text{cm}^{-1}$ , green) and the nitrile signal (2226–2276  $\text{cm}^{-1}$ , red) were both clearly observed with some region superimposed, as shown in the merged image (first panel of Figure 3b). Three different locations in the merged image had thus been selected for comparing the SERS spectra, in which point 1 had a unique peak at around 2251  $\text{cm}^{-1}$ , indicating the existence of nanoprobe agglomerates, but unlikely due to the dopamine bridging. Point 2 had a clear peak only at around 1595  $\text{cm}^{-1}$ , which might be ascribed to

other unspecific benzene-containing substances in the cytoplasm, while point 3 had two main peaks at both positions, expected to be the area of interests where dopamine was presented (Figure 3c). Notably, dopamine was found only in the cytoplasm of PC12 cells. It could be simply ascribed to the exclusion of nanoparticles into the cell nucleus. As controls, the functionalized BME/SPN-Au and DSP/SPN-Au were also testified in the living cells in order to avoid any undesired false results. Although the SERS images were obtained in the same way, the signals in both channels were much less than BME/DSP/SPN-Au. Any overlap could be barely seen in the merged images (third and fourth panels, Figure 3b). The nitrile channel image of BME/SPN-Au suggested that there was still some occurrence of nanoparticle agglomeration, perhaps due to the nonspecific binding, which however was not observed for DSP/SPN-Au-treated cells. Other controls such as cells preincubated with citrate-capped AuNPs and without AuNPs were also imaged, which did not show any dopamine specific signal (Figure S5a). Additionally, in order to prove the dopamine imaging ability of our nanoprobes, an endogenous agonist peptide (ghrelin) was used to treat PC12 cells to excrete dopamine for maintaining a low level of dopamine in the cytoplasm.<sup>25</sup> As expected, the interested signals in SERS images of the treated PC12 cells were much reduced (second panel, Figure 3b), thus confirming the specific dopamine imaging ability by using BME/DSP/SPN-Au.

Images containing multiple cells were taken and analyzed to demonstrate the overall performance of our nanoprobes for cellular dopamine sensing (Figure S6). Basically, the same results could be observed in a larger area. Further statistical studies were also carried out. Briefly, all pixels with their Raman spectra in the acquired images were screened first to eliminate the background pixels, which failed to show any pronounced peaks rather than just noise. Note that the background pixels are defined as the positions, in which less than 50 data points in the whole Raman spectra (total 1015 data points within 1317–2331  $\text{cm}^{-1}$ ) showed intensities higher than 100 arbitrary unit (a.u.). A minority of pixels ( $\sim 10\%$ ) were valid for the composition of data points ( $x, y$ ), where  $x$  and  $y$  represented the intensity integrals in 1570–1620 and 2226–2276  $\text{cm}^{-1}$  channels of Raman spectra of each pixel, respectively. A total of around 600 data points of each group including the designed dopamine nanoprobes and controls were then randomly selected and are plotted in Figures 3d,e and S5b. The point distributions of each group show differences, as the points of BME/DSP/SPN-Au in normal PC12 cells (black squares) and in treated cells (red circles) spread more widely than other controls. The points of BME/SPN-Au showed a more clustered pattern with a higher intensity in the 2226–2276  $\text{cm}^{-1}$  channel (green diamonds), whereas the points of DSP/SPN-Au spread as a belt across the 1570–1620  $\text{cm}^{-1}$  channel (blue triangles). In order to give a quantitative illustration, we set the threshold value of 1000 for both channels (gray broken line, Figure 3d,e), so that all points could be classified into four quadrants. Table S1 summarizes the actual percentages of each quadrant for all groups, in which the percentages of the double-positive signal clearly showed a decreasing trend from BME/DSP/SPN-Au in normal PC12 cells (23.8%) to that in treated PC12 cells (15.5%), indicating the decrease of cellular dopamine levels. Other controls showed minimal signal levels (e.g., 6.0% for DSP/SPN-Au and 6.3% for BME/SPN-Au, both in normal PC12 cells), suggesting that they were not capable of cellular dopamine

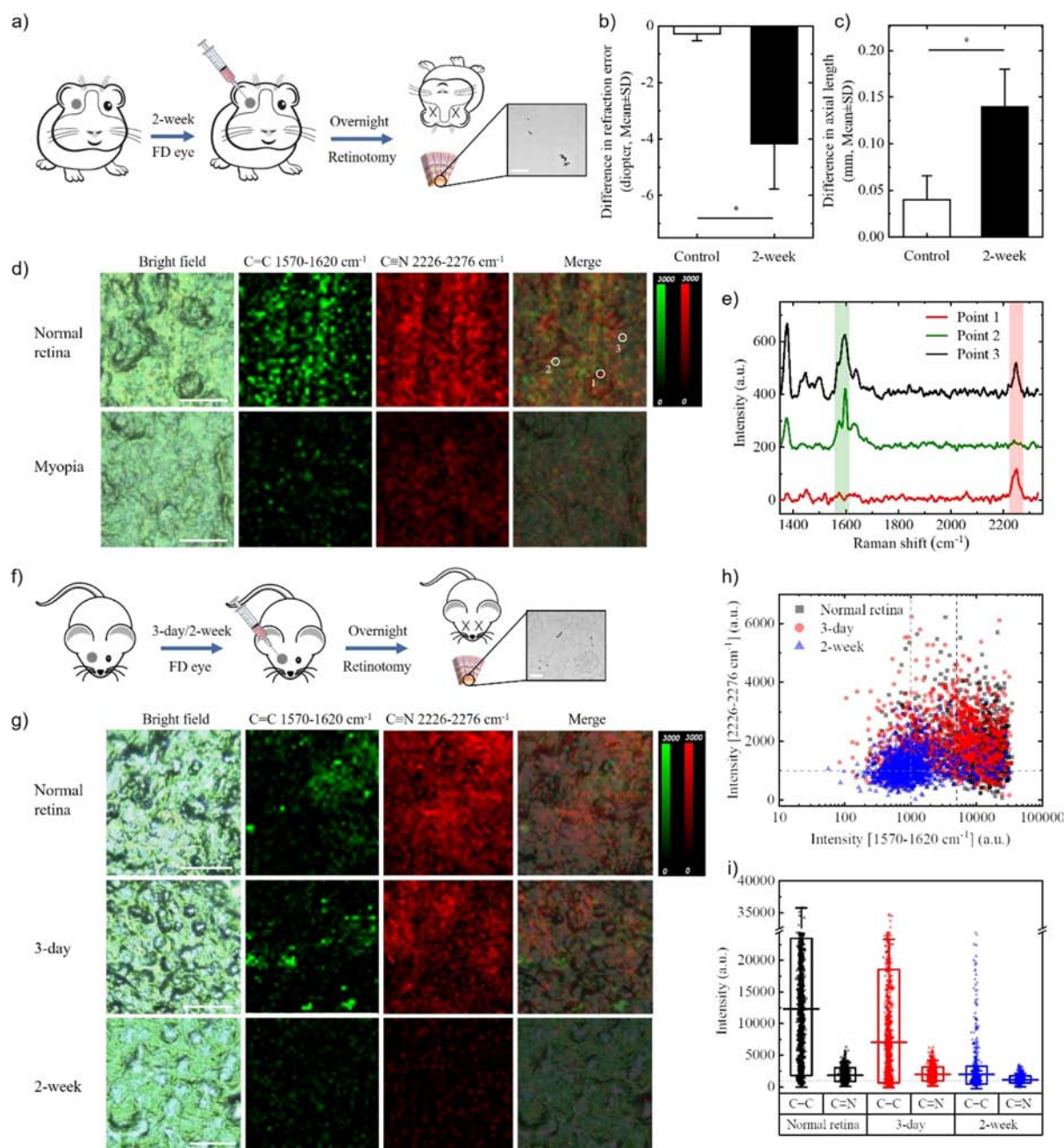


**Figure 4.** SERS imaging analysis of dopamine in mice retina injected with functional nanoprobe. Schematic illustration for the preparation of (a) guinea pig and (f) mice retinal whole mount injected with BME/DSP/SPN-Au prior to Raman imaging. Inset: TEM images of intracellular nanoprobe; scale bar: 500 nm. (b) Optical measurements of refraction in the myopia model treated with 2-week FD and control ( $n = 12$ ). (c) Measurements of ocular axial length in the myopia model treated with 2-week FD and control ( $n = 12$ ). Bright-field, SERS mapping images of retinal tissues acquired in 1570–1620 and 2226–2276  $\text{cm}^{-1}$  channels and their merged images. (d) Guinea pig: top, normal retina images and bottom: retina from the myopia model. (e) SERS spectra of point 1, point 2, and point 3 in (d). (h) Scatter plot of pixel intensities in Raman images of the normal retinal tissue (black squares), and retina from 3-day (red dots), and 2-week (blue triangles) FD models of mice. (i) Box plot of pixel intensities in Raman images of the normal retinal tissue (black squares) and retina from 3-day (red dots) and 2-week (blue triangles) FD models. Within each group, the left and right boxes showed the averaged intensities in 1570–1620  $\text{cm}^{-1}$  (C=C) and 2226–2276  $\text{cm}^{-1}$  (C=N) channels, respectively.

detection (Figure 3f). Instead of percentages, the averaged values of each group were calculated and compared as well. By using BME/DSP/SPN-Au, the averaged values for both channels in normal PC12 cells were significantly higher than the ones in treated cells and two other controls (Figure 3g). All the derived data were consistent with previous imaging results. Therefore, the SERS nanoprobe for dopamine imaging in the

living cells had been successfully demonstrated with high specificity in a relatively large area of interest.

**Dopamine Imaging in the Retinal Tissue.** It is important to know the spatial distributions of dopamine in the retinal tissue, as the functionalities of dopamine vary.<sup>5</sup> Bearing the excellent tissue compatibility of Raman-related methods reported by previous works for *in vivo* human retina

detection,<sup>26,27</sup> we further applied our SERS nanoprobe for dopamine imaging in the retinal tissues and hopefully would be used in future for the *in vivo* tests.

Retina from guinea pigs was first examined to verify the performance of SERS nanoprobe in tissue dopamine imaging. The right eye of guinea pigs in the FD group was covered by a translucent lens for 2 weeks to develop myopia, followed by the injection of nanoprobe to both eyes. After an overnight incubation, the guinea pigs were sacrificed and the retinotomy was performed to obtain the fresh retinal whole mount, on which the Raman imaging was recorded and the signals were enhanced by cellular nanoprobe, as shown in the TEM image (Figure 4a). The formation of experimental myopia was confirmed by refraction and ocular axial length measurements (Figure 4b,c). The bright-field images of the retinal tissues from the normal and FD group (myopia) did not show any clear difference (Figure S7a), while the Raman images of the two interested channels (1570–1620 and 2226–2276  $\text{cm}^{-1}$ ) varied significantly (Figure 4d). There was a massive distribution of both signals in normal retina as compared to the FD group (myopia, Figure 4d) and the control sample without AuNPs (Figure S7b). Three points were circled to illustrate the Raman spectra for different locations, among which point 3 showed peaks at both channels indicating the existence of dopamine, while other two points showed only one peak at either channel (Figure 4e).

A total of around 1200 data points extracted from acquired Raman images of each group were plotted (Figure S8a). The normal group (black squares) spreads more widely toward the higher values than the myopia group (red circles). The threshold value of 1000 was continuously used to divide the plot into four quadrants. The percentages of each group according to the thresholds are recorded in Table S2, showing that the double-positive percentage (87.0%) of the normal group was significantly larger than that of the myopia group (45.5%). Different from the living cells, the average intensity at 1570–1620  $\text{cm}^{-1}$  was more than twofold higher in retinal tissues, which might be ascribed to the complex environment of tissues. The threshold value of the 1570–1620  $\text{cm}^{-1}$  channel thus changed to 5000 in order to accurately evaluate the level of dopamine. As a result, the percentages of double-positive signals of both groups dropped, but with an enlarged fourfold gap (42.9 and 10.6%, respectively, Table S2). Meanwhile, the averages of intensity integrals showed significantly higher values in normal retina than myopia ones (Figure S8b). The following HPLC measurement strongly supported the Raman image analysis (Figure S8c) and was consistent with previous studies as well.<sup>9</sup> It could therefore be concluded that our SERS nanoprobe work well for the dopamine imaging in retinal tissues.

Different from guinea pigs, the dopamine level associated with myopia in the mice model was not well studied.<sup>28</sup> Therefore, the SERS nanoprobe was further applied in the mice retina. Similar procedures were conducted to the mice for the development of FD myopia with 3-day or 2-week treatments, and the averaged content of gold was about 176.8 ng per retina as determined by ICP-MS measurements (Figure 4f). The injected nanoprobe had successfully penetrated retinal cells as in the guinea pig model, observed in the TEM image of the retinal slices (inset, Figure 4f). The FD model of mice after 2-week treatment was confirmed in optical refraction measurements showing a clear decrease in diopter, while 3-day treatment was not significant (Figure S9a).

However, both FD treatments failed to show an extended ocular axial length than the control ones (Figure S9b). All three groups of retinas (normal, 3-day, and 2-week FD treatments) had no observable difference in the bright-field images (bright field, Figure S10a). Nevertheless, the SERS images showed a trend of decreasing signals after the development of FD in both interested channels (Figure 4g), suggesting the decreasing levels of dopamine. Especially for the 2-week treatment group, there was almost no local dopamine detected in the Raman images, which appeared similarly as the negative control (Figure S10b). Interestingly, the HPLC analysis of the total dopamine amount in mice retina did not show a significant difference for both FD models (3-day and 2-week) from their controls in contrast to our assay (Figure S9c). It could be the reason that our assay mainly reflected the localized dopamine (with each measured area of  $\sim 0.0025 \text{ mm}^2$ , about 1/6000 of the whole mount retina) rather than the total retinal dopamine, potentially providing more details of local dopamine levels and distributions for myopia studies in the mice model.

The followed statistical analysis was done in the same way as previous protocols. As shown in Figure 4h, the normal and 3-day groups were hardly distinguishable mainly localizing at the double-positive area (black squares and red circles), whereas the 2-week group shrank more into the negative area (blue triangles). After dividing the plot into four quadrants with threshold values set at 1000, the percentages of each are summarized in Table S3, in which the percentage of double positives could be utilized to indicate the dopamine levels arbitrarily. Similar as in guinea pigs' models, the background noises in the 1570–1620  $\text{cm}^{-1}$  channel were elevated, which could possibly hinder the differences among groups. The threshold value of the 1570–1620  $\text{cm}^{-1}$  channel was then selected to be 5000. The percentages of double positives dropped accordingly: 79.0 to 62.4% in the normal group, 70.2 to 42.3% in the 3-day group, and 25.2 to 4.3% in the 2-week group, while the intergroup differences increased (Table S3). In particular, the differences between normal retinas and 3-day FD ones changed from 8.8% (1000 a.u.) to 20.1% (5000 a.u.), greatly extending the dopamine sensing range in tissues. The averaged intensities of all three groups were calculated, collectively showing a consistent result of decreasing dopamine levels after FD treatments (Figure 4i). Therefore, it could be concluded that the dopamine levels of mice retina decreased after 2-week FD treatment according to the SERS imaging by our nanoprobe, which had not been reported by other means in mice.<sup>8,28</sup> Our approach suggested a new way of sensing local dopamine in retina, which was suitable for studying relations between dopamine and various eye diseases in different animal models.

## CONCLUSIONS

In this work, we had successfully developed a SERS nanoprobe for dopamine imaging in retinal tissues. The rational designed plasmonic nanoprobe, BME/DSP/SPN-Au, were verified in both colorimetric and SERS assays, which could also be applied in field tests at remote areas performed by untrained personnel. The high sensitivity down to the nanomolar range with high specificity was achieved by SERS assays enabling the further cellular and retinal dopamine imaging, where the dopamine distribution had been revealed inside the cells. After successful demonstration of the declined retinal dopamine level in the myopia model of guinea pigs with our SERS

nanoprobes, the mice FD models were studied subsequently. In our assay, the results suggested that the retinal dopamine level dropped in the FD models of mice as compared to the normal ones. The reported SERS nanoprobe for dopamine detection and imaging at retina enabled the local dopamine sensing at the cellular level and paved a way for further *in vivo* dopamine tests upon considering the laser safety and the fundamental studies in diagnostic and treatment of dopamine-related diseases. Alternatively, the SERS imaging platform could be further applied to other small molecule detection in the real biological samples depending on the specific functionalization of nanoprobes.

## ■ ASSOCIATED CONTENT

### SI Supporting Information

The Supporting Information is available free of charge at <https://pubs.acs.org/doi/10.1021/acs.analchem.1c01108>.

Additional experimental details, materials and methods, additional characterizations of functional nanoprobes, cellular and retinal imaging analysis, and characterizations of model animals and statistical tables (PDF)

## ■ AUTHOR INFORMATION

### Corresponding Authors

**Hao Chen** – School of Biomedical Engineering, School of Ophthalmology & Optometry, Wenzhou Medical University, Wenzhou 325027, China; Email: [chenhao@mail.eye.ac.cn](mailto:chenhao@mail.eye.ac.cn)

**Xiaohu Liu** – School of Biomedical Engineering, School of Ophthalmology & Optometry, Wenzhou Medical University, Wenzhou 325027, China; Wenzhou Institute, University of Chinese Academy of Sciences, Wenzhou 325001, China; [orcid.org/0000-0002-0892-7172](https://orcid.org/0000-0002-0892-7172); Email: [liuxiaohu@wmu.edu.cn](mailto:liuxiaohu@wmu.edu.cn)

**Yi Wang** – School of Biomedical Engineering, School of Ophthalmology & Optometry, Wenzhou Medical University, Wenzhou 325027, China; Wenzhou Institute, University of Chinese Academy of Sciences, Wenzhou 325001, China; [orcid.org/0000-0002-2110-623X](https://orcid.org/0000-0002-2110-623X); Email: [wangyi@wiucas.ac.cn](mailto:wangyi@wiucas.ac.cn)

### Authors

**Xueqian Ren** – School of Biomedical Engineering, School of Ophthalmology & Optometry, Wenzhou Medical University, Wenzhou 325027, China; Wenzhou Institute, University of Chinese Academy of Sciences, Wenzhou 325001, China

**Qingwen Zhang** – School of Biomedical Engineering, School of Ophthalmology & Optometry, Wenzhou Medical University, Wenzhou 325027, China; Wenzhou Institute, University of Chinese Academy of Sciences, Wenzhou 325001, China

**Jinglei Yang** – School of Biomedical Engineering, School of Ophthalmology & Optometry, Wenzhou Medical University, Wenzhou 325027, China

**Xinjuan Zhang** – Wenzhou Institute, University of Chinese Academy of Sciences, Wenzhou 325001, China

**Xueming Zhang** – Wenzhou Institute, University of Chinese Academy of Sciences, Wenzhou 325001, China

**Yating Zhang** – Department of Electronic Engineering, Tsinghua University, Beijing 100084, China

**Liping Huang** – School of Biomedical Engineering, School of Ophthalmology & Optometry, Wenzhou Medical University, Wenzhou 325027, China; Wenzhou Institute, University of Chinese Academy of Sciences, Wenzhou 325001, China

**Changshun Xu** – School of Biomedical Engineering, School of Ophthalmology & Optometry, Wenzhou Medical University, Wenzhou 325027, China; Wenzhou Institute, University of Chinese Academy of Sciences, Wenzhou 325001, China

**Yuancai Ge** – School of Biomedical Engineering, School of Ophthalmology & Optometry, Wenzhou Medical University, Wenzhou 325027, China; Wenzhou Institute, University of Chinese Academy of Sciences, Wenzhou 325001, China

Complete contact information is available at:

<https://pubs.acs.org/doi/10.1021/acs.analchem.1c01108>

### Author Contributions

<sup>†</sup>X.R., Q.Z., and J.Y. contributed equally to this work.

### Notes

The authors declare no competing financial interest.

## ■ ACKNOWLEDGMENTS

This work was financially supported by National Key R&D Program of China (2017YFC0111300), Zhejiang Province Natural Science Fund for Distinguished Young Scholars (LR19H180001), Leading Talent Innovation and Entrepreneurship Project of Wenzhou (RX2016005), and Public Projects of Wenzhou (2020005).

## ■ REFERENCES

- (1) Klein, M. O.; Battagello, D. S.; Cardoso, A. R.; Hauser, D. N.; Bittencourt, J. C.; Correa, R. G. *Cell. Mol. Neurobiol.* **2019**, *39*, 31–59.
- (2) Pan, X.; Kaminga, A. C.; Wen, S. W.; Wu, X. Y.; Acheampong, K.; Liu, A. Z. *Front. Aging Neurosci.* **2019**, *11*, 175.
- (3) Yang, P.; Perlmutter, J. S.; Benzinger, T. L. S.; Morris, J. C.; Xu, J. *Ageing Res. Rev.* **2020**, *57*, 100994.
- (4) Howes, O. D.; McCutcheon, R.; Owen, M. J.; Murray, R. M. *Biol. Psychiatr.* **2017**, *81*, 9–20.
- (5) Witkovsky, P. *Doc. Ophthalmol.* **2004**, *108*, 17–39.
- (6) Wong, T. Y.; Ferreira, A.; Hughes, R.; Carter, G.; Mitchell, P. *Am. J. Ophthalmol.* **2014**, *157*, 9–25.
- (7) Holden, B. A.; Fricke, T. R.; Wilson, D. A.; Jong, M.; Naidoo, K. S.; Sankaridurg, P.; Wong, T. Y.; Naduvilath, T. J.; Resnikoff, S. *Ophthalmology* **2016**, *123*, 1036–1042.
- (8) Zhou, X.; Pardue, M. T.; Iuvone, P. M.; Qu, J. *Prog. Retin. Eye Res.* **2017**, *61*, 60–71.
- (9) Zhang, S.; Yang, J.; Reinach, P. S.; Wang, F.; Zhang, L.; Fan, M.; Ying, H.; Pan, M.; Qu, J.; Zhou, X. *Invest. Ophthalmol. Vis. Sci.* **2018**, *59*, 4441–4448.
- (10) Pérez-Jiménez, A. I.; Lyu, D.; Lu, Z.; Liu, G.; Ren, B. *Chem. Sci.* **2020**, *11*, 4563–4577.
- (11) Zong, C.; Xu, M.; Xu, L.-J.; Wei, T.; Ma, X.; Zheng, X.-S.; Hu, R.; Ren, B. *Chem. Rev.* **2018**, *118*, 4946–4980.
- (12) Zeng, Y.; Ren, J.-Q.; Shen, A.-G.; Hu, J.-M. *J. Am. Chem. Soc.* **2018**, *140*, 10649–10652.
- (13) Lee, H. K.; Lee, Y. H.; Koh, C. S. L.; Phan-Quang, G. C.; Han, X.; Lay, C. L.; Sim, H. Y. F.; Kao, Y.-C.; An, Q.; Ling, X. Y. *Chem. Soc. Rev.* **2019**, *48*, 731–756.
- (14) Liu, X.; Zhang, Q.; Knoll, W.; Liedberg, B.; Wang, Y. *Adv. Mater.* **2020**, *32*, 2000866.
- (15) Liu, X.; Wang, Y.; Chen, P.; McCadden, A.; Palaniappan, A.; Zhang, J.; Liedberg, B. *ACS Sens.* **2016**, *1*, 1416–1422.
- (16) Liu, X.; Wang, Y.; Chen, P.; Wang, Y.; Zhang, J.; Aili, D.; Liedberg, B. *Anal. Chem.* **2014**, *86*, 2345–2352.
- (17) Wang, Y.; Liu, X.; Zhang, J.; Aili, D.; Liedberg, B. *Chem. Sci.* **2014**, *5*, 2651–2656.
- (18) Zhang, J.; Wang, Y.; Wong, T. I.; Liu, X.; Zhou, X.; Liedberg, B. *Nanoscale* **2015**, *7*, 17244–17248.
- (19) Li, M.; Li, J.; Di, H.; Liu, H.; Liu, D. *Anal. Chem.* **2017**, *89*, 3532–3537.

- (20) Kong, B.; Zhu, A.; Luo, Y.; Tian, Y.; Yu, Y.; Shi, G. *Angew. Chem. Int. Ed.* **2011**, *50*, 1837–1840.
- (21) Chithrani, B. D.; Chan, W. C. W. *Nano Lett.* **2007**, *7*, 1542–1550.
- (22) Chen, P.; Liu, X.; Goyal, G.; Tran, N. T.; Shing Ho, J. C.; Wang, Y.; Aili, D.; Liedberg, B. *Anal. Chem.* **2018**, *90*, 4916–4924.
- (23) Olefirowicz, T. M.; Ewing, A. G. *J. Neurosci. Methods* **1990**, *34*, 11–5.
- (24) Greene, L. A.; Tischler, A. S. *Proc. Natl. Acad. Sci. U.S.A.* **1976**, *73*, 2424–2428.
- (25) Nanmoku, T.; Takekoshi, K.; Ishi, K.; Kawakami, Y.; Isobe, K.; Shibuya, S.; Okuda, Y.; Nakai, T. *Endocr. Res.* **2003**, *29*, 17–21.
- (26) Gellermann, W.; Ermakov, I. V.; Ermakova, M. R.; McClane, R. W.; Zhao, D.-Y.; Bernstein, P. S. *J. Opt. Soc. Am. A* **2002**, *19*, 1172–1186.
- (27) Stiebing, C.; Schie, I. W.; Knorr, F.; Schmitt, M.; Keijzer, N.; Kleemann, R.; Jahn, I. J.; Jahn, M.; Kiliaan, A. J.; Ginner, L.; Lichtenegger, A.; Drexler, W.; Leitgeb, R. A.; Popp, J. *Neurophotonics* **2019**, *6*, 041106.
- (28) Wu, X.-H.; Li, Y.-Y.; Zhang, P.-P.; Qian, K.-W.; Ding, J.-H.; Hu, G.; Weng, S.-J.; Yang, X.-L.; Zhong, Y.-M. *Invest. Ophthalmol. Vis. Sci.* **2015**, *56*, 967–977.